energies

MDPI

Article

The Diagnosis of Shunt Defects in CIGS Modules Using Lock-In Thermography: An Empirical Comparative Study

Seung Hoon Lee [1], Hae-Seok Lee [2], Donghwan Kim [1] and Yoonmook Kang [2,*]

[1] Department of Material Science and Engineering, Korea University, Seoul 02841, Republic of Korea; steve880627@korea.ac.kr (S.H.L.); donghwan@korea.ac.kr (D.K.)
[2] Graduate School of Energy and Environment (KU-KIST Green School), Korea University, Seoul 02841, Republic of Korea; lhseok@korea.ac.kr
* Correspondence: ddang@korea.ac.kr

Abstract: Shunt defects are often detected in solar panels intended for photovoltaic applications. However, existing nondestructive detection technologies have certain inherent drawbacks depending on the application scenario. In this context, this paper reports a comprehensive empirical investigation into lock-in thermography (LIT) and its applicability to diagnosing shunt defects in copper indium gallium selenide (CIGS) solar modules. LIT was compared with biased thermography, and its distinctive attributes were elucidated. The comparison results demonstrate the superior capabilities of LIT at enhancing the signal-to-noise ratio, improving the visibility, resolution, and quantification of defects, and highlighting the usefulness of LIT for advanced defect analysis. We explored scenarios in which biased thermography could be appropriate despite its inherent limitations and identified conditions under which it might be preferred. The complex thermal behavior of different types of defects under various voltage conditions was analyzed, contributing to a more nuanced understanding of their behavior. Thus, integrating experimental results and theoretical understanding, we provide valuable insights and scientific guidelines for photovoltaic research. Our findings could help enhance the efficiency of defect detection in CIGS modules, highlighting the critical role of optimized thermographic techniques in developing photovoltaic technologies.

Keywords: CIGS solar module; lock-in thermography; shunt defect; thin-film photovoltaics

check for updates

Citation: Lee, S.H.; Lee, H.-S.; Kim, D.; Kang, Y. The Diagnosis of Shunt Defects in CIGS Modules Using Lock-In Thermography: An Empirical Comparative Study. *Energies* **2023**, *16*, 7226. https://doi.org/10.3390/en16217226

Academic Editors: Peter D. Lund, Philippe Leclère and Jeff Kettle

Received: 15 August 2023
Revised: 23 September 2023
Accepted: 23 October 2023
Published: 24 October 2023

Copyright: © 2023 by the authors. Licensee MDPI, Basel, Switzerland. This article is an open access article distributed under the terms and conditions of the Creative Commons Attribution (CC BY) license (https://creativecommons.org/licenses/by/4.0/).

1. Introduction

Considering that solar cells are vital components of photovoltaic systems, they are being rapidly developed, with their performance, longevity, and reliability fundamentally determined by the quality of their constitutive materials and the precision of manufacturing processes. However, various types of mechanical defects have been found in solar cells, thus making the identification and characterization of such defects, particularly shunt defects, a critical concern in the field of photovoltaics. Among nondestructive testing methodologies, thermography has emerged as a compelling tool for this task, with two primary techniques gaining prominence: biased thermography and lock-in thermography (LIT) [1–6].

Biased thermography, known as quasi-steady-state thermography, monitors temporal temperature variations by applying a continuous electrical bias, whereas LIT synchronizes the thermal signal with the modulation frequency to improve the signal-to-noise ratio. Despite the superior resolution offered by LIT, its application is limited by the need for sophisticated and expensive equipment [5,6].

Diagnostic strategies, including thermography, can find applications in various photovoltaic devices, such as silicon-based and perovskite solar modules, particularly in copper indium gallium selenide (CIGS) solar modules. However, each material and architecture presents unique challenges, with the results affected by the inherent material properties and

defect type. Thus, recognizing these nuances is paramount to effectively apply diagnostic techniques across a wide variety of photovoltaic devices [5–9].

Recent studies have provided a better understanding of the application of these techniques. For instance, Fecher et al. demonstrated how imaging illuminated LIT could be combined with 2D electrical simulations for effective loss analysis in CIGS modules [10], followed by complementary studies such as those of Guthrey et al., who focused on the reverse-bias breakdown in CIGS photovoltaic devices, and Aninat et al. and Palmiotti et al., who provided detailed examinations of defects in CIGS PV modules [11–13]. These studies collectively represent the state-of-the-art in nondestructive defect detection and have contributed to the methodological discourse in the field.

However, there remains a challenge in many laboratories where commercially available LIT systems are used without a comprehensive understanding of the respective strengths and drawbacks of each method. This study aimed to address this knowledge gap by conducting a comparative analysis of biased thermography and LIT, focusing on investigating shunt defects in CIGS modules [4–19].

We present an analysis of a CIGS mini-module by employing a system capable of both biased thermography and LIT. Through a comparison analysis, we demonstrate the efficacy of these two techniques and identify scenarios in which biased thermography performed adequately [4–19]. We also provide an in-depth discussion of the advantages and limitations of each thermography method when diagnosing shunt defects in CIGS modules. In addition, practical guidelines for selecting and optimizing a suitable technique for specific applications are suggested. Hence, this paper contributes to ongoing research in improving the quality and performance of CIGS modules in the field of photovoltaics, including potential future directions in this area.

2. Materials and Methods

2.1. Sample Preparation

CIGS mini-module samples were prepared over several stages. First, a molybdenum back-contact layer was deposited on a soda-lime glass substrate via direct current magnetron sputtering. Subsequently, the first pattern (P1) for the monolithically integrated photovoltaic module design was generated using picosecond laser scribing. Thereafter, a Cu–In–Ga-mixed oxide (CIGOx) layer with a thickness of 1 µm was deposited through iterative spin-coating using an alcohol-based precursor solution, followed by simultaneous selenization and sulfurization. A CdS buffer layer of 50 nm thickness was subsequently grown on the CIGS layer via chemical bath deposition, followed by the deposition of a 50 nm-thick intrinsic zinc oxide (i-ZnO) layer through radio frequency (RF) magnetron sputtering. The second pattern (P2) was achieved using a mechanical scribing method, which facilitated the series connection of consecutive unit cells, resulting in four unit cells connected in series within the mini-module sample. An aluminum-doped zinc oxide (Al:ZnO) layer with a thickness of 500 nm was deposited as a transparent conductive oxide layer using RF sputtering. The third pattern (P3) was applied via a mechanical scriber to ensure the isolation of each unit cell within the modules. The sample preparation process is detailed in our previous report [12].

2.2. Thermography Characterization

Utilizing an FLIR A655sc thermographic camera with a frame rate of up to 50 Hz, both biased thermography and dark lock-in thermography (DLIT) techniques were employed to identify the shunt sites within the samples. A Keithley 2651A source meter was used to facilitate the application of several bias voltage conditions, with a maximum reverse bias of −8 V and a maximum forward bias of +7 V. The lock-in parameters, including the frequency (1 Hz) and the number of loops (20), were specifically adjusted to effectively investigate thermal signals in relation to shunt defects, with amplitude images utilized to display the lock-in thermography results. Notably, the emissivity setting for the position of the sample and the temperature setting for the camera detector were not utilized because

they were determined to be noncritical parameters in the context of shunt defect detection. More detail on the fundamentals of LIT can be found in previous works [5,6].

3. Results

Figure 1 shows the results of our experimentation using both biased and LIT techniques. Figure 1a shows a thermographic image of a CIGS mini-module sample subjected to a bias of −6 V. This image primarily demonstrates the temperature resolution or detection limit of the IR camera, indicating that only signals surpassing the noise amplitude can be detected.

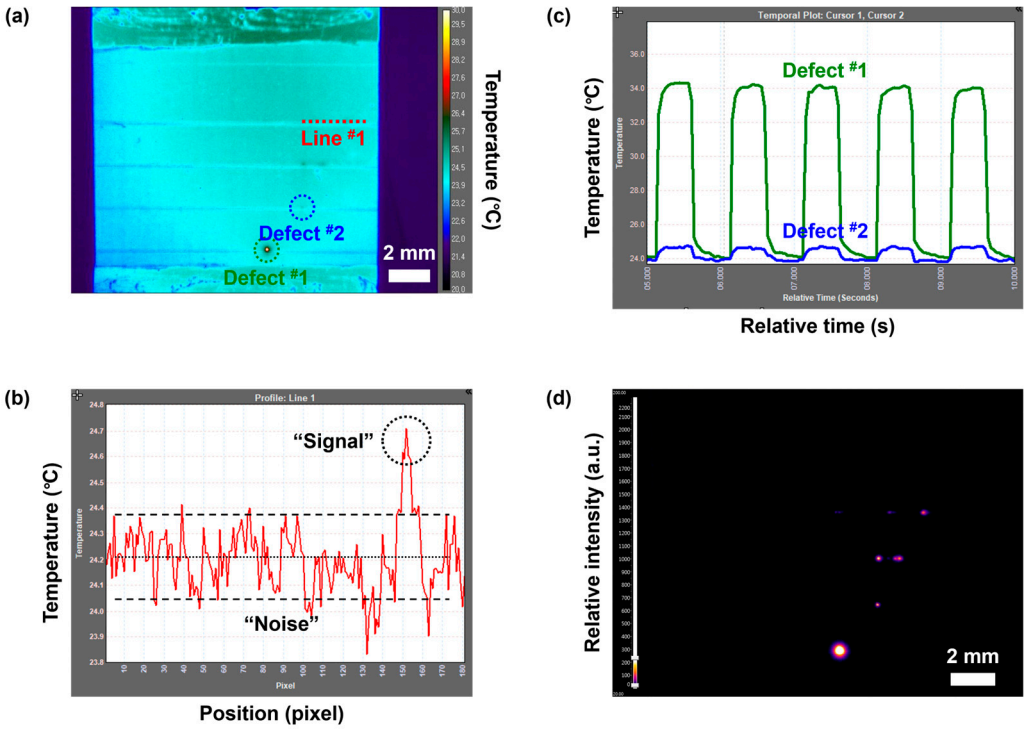

Figure 1. Examination of passive and lock-in thermography techniques applied to a CIGS mini-module sample subjected to a −6 V bias: (**a**) Passive thermographic image delineating the temperature resolution of the IR camera, with a detectable threshold set above the noise level; (**b**) Temperature profile across a linear region of interest (ROI), marked in red in (**a**), illustrating noise as random fluctuations independent of the applied bias; (**c**) Temporal temperature variations for ROI identified as defects #1 and #2 in (**a**), exhibiting the effect of the pulsed bias; (**d**) Lock-in thermography analysis revealing enhanced signal-to-noise ratio and improved image clarity in comparison to passive thermography.

Figure 1b shows the temperature profile for line-shaped regions of interest (ROI), highlighted in red in Figure 1a, indicating that random fluctuations, approximately 0.2 °C at 24.2 °C, arise independently of the applied bias and can, thus, be classified as noise. Temperature signals exceeding this noise level can be detected using biased thermography. In the example given in Figure 1b, biased thermography detected a shunt site signal at 24.7 °C, while signals within the noise range remained indistinguishable.

Previous observation results showed that biased thermography has several limitations: first, for a signal to be detected, it must be of sufficient strength. Second, thermal dispersion from distinct shunt sites can decrease the spatial resolution as adjacent areas heat up simultaneously over time. Finally, applying a continuous bias may damage the sample at high temperatures. A pulsed bias was applied to mitigate these limitations. Figure 1c presents the temporal temperature profiles for ROIs labeled as defects #1 and #2 in Figure 1a,

indicated by the green and blue markers, respectively. The temperature fluctuations in response to the pulsed bias are distinctly visible in these profiles.

LIT can be executed by repeating this process and gathering multiple images. Figure 1d presents the outcome of an LIT analysis conducted on the data shown in Figure 1a. Applying the lock-in technique yielded a high signal-to-noise ratio, resulting in clear and reliable images. Overall, these results demonstrate the superior capabilities of lock-in thermography in relation to biased thermography, particularly in terms of the signal-to-noise ratio and spatial resolution.

Figure 2 shows a simplified representation of the LIT principle, illustrated in a matrix format. Each matrix element represents the temperature of an individual pixel, with changes occurring either in response to the applied pulsed bias or independently. These temperature changes induced by the applied bias are characterized as signal components, whereas random temperature fluctuations are considered noise.

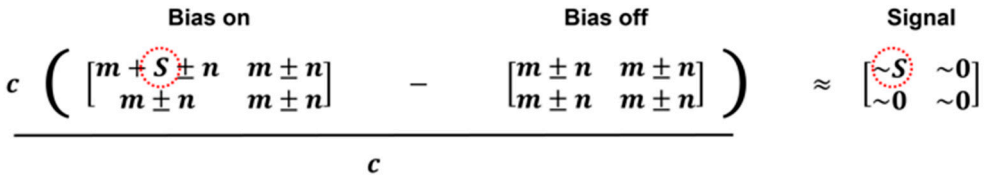

Figure 2. Matrix representation of the lock-in thermography (LIT) algorithm, illustrating the extraction of signal components and minimization of noise using a pulsed bias. The elements of the matrix—*S*, *n*, *m*, and *c*—denote the additional signal, noise dispersion, mean temperature, and number of measurement cycles, respectively. This matrix approach shows the mechanism by which LIT improved the signal-to-noise ratio and elucidated signal fluctuations within thermal images.

The noise dispersion, indicated by *n*, diverges randomly from the mean temperature value and approximately aligns with temperature resolution. By contrast, the mean temperature value of a particular pixel, designated by *m*, remains constant throughout the measurements. If the temperature of a pixel varies differently from the applied bias, this additional temperature change is denoted by *S*, highlighting the presence of additional signals in these pixels. To optimize the signal-to-noise ratio, the number of measurement cycles, denoted as *c*, should be high.

The advantage of this matrix representation becomes apparent in the LIT process, where thermal images are continuously acquired in response to an external pulsed bias. Once these images are collected, the time-dependent thermal changes captured in the images are Fourier-transformed into frequency-dependent thermal signals. This essential step in the lock-in principle enables the clear extraction and isolation of significant signal components amidst the noise. Consequently, this combined process facilitates improved noise reduction and signal extraction, highlighting the effectiveness of the LIT methodology [5,6].

Figure 3 shows a comparison between biased thermography and LIT. Both techniques were applied to a CIGS mini-module sample under a +3 V voltage and visually compared through thermographic and LIT images, each presented with a different scale. Specifically, Figure 3a–c show the thermographic images at varying temperature scales of −21.5–24, 20–28, and 15–35 °C, respectively. Figure 3d,e show LIT images with signal scales of −0–200 and 20–200 arbitrary units, respectively.

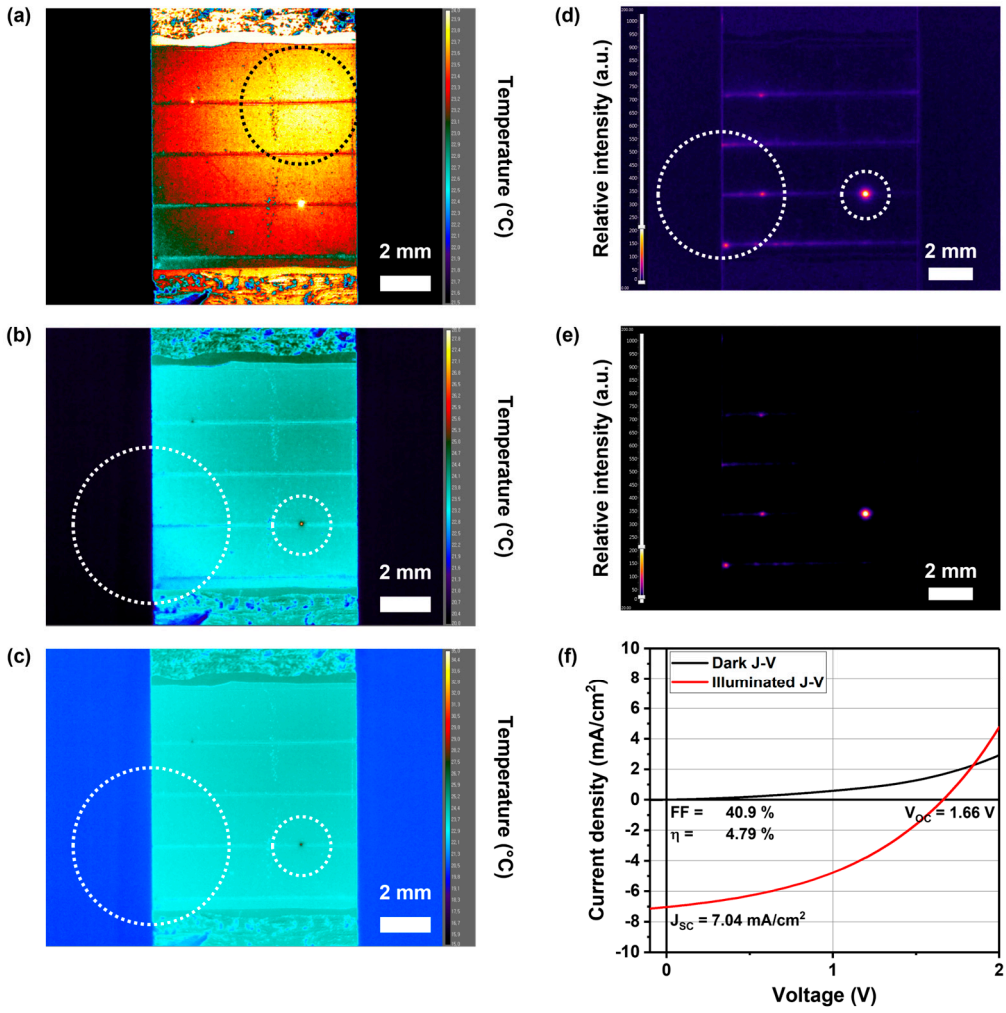

Figure 3. Side-by-side comparison of biased thermography and lock-in thermography (LIT) when applied to a CIGS mini-module sample with an area of 2.4 cm^2 under +3 V bias. The figures show thermographic images (**a**–**c**) in the temperature scales of 21.5–24, 20–28, and 15–35 °C, respectively. The black circle in (**a**) indicates the biased baseline, or "Narcissus effect". By comparison, LIT images (**d**,**e**) in the signal scales of 0–200 and 20–200 arbitrary units reveal the ability of LIT to capture subtler signals, as shown in (**d**), and eliminate baseline bias, as illustrated in (**e**). (**f**) J–V characteristics of the corresponding module sample.

In Figure 3a, the area enclosed by a black circle has a higher temperature than its surroundings. However, this temperature increase did not result from a shunt site signal caused by an externally applied bias but arose from a biased baseline originating from the measurement environment, known as the "Narcissus effect". This unforeseen noise or bias can be suppressed by adjusting the temperature scale when the degree of bias is low. As shown in Figure 3b,c, widening the temperature scale can reduce the relative strength of bias. However, this strategy inherently weakens the relative strength of the signal, making shunt sites with subtle signals invisible.

As an example, in Figure 3d, the defect, which has a weak signal, highlighted within the large white circle on the left, is only visible in the LIT image. By comparison, the shunt site indicated within the small white circle on the right is visible in both the biased thermography and LIT images, owing to its robust signal.

Notably, LIT isolates the signal due to the thermal change depending directly on the intentionally applied bias, eliminating the baseline bias seen in Figure 3a and making only the true signal visible, as shown in Figure 3e. This unique aspect of LIT reduces the need for stringent control of the measurement environment to reduce unintentional bias.

In the results illustrated in Figure 3a–e, both the biased thermography and LIT images clearly show the presence of shunt sites within the module sample; this is particularly evident in the LIT image, where the bright regions indicate these shunt sites. The illuminated J–V curve in Figure 3f exhibits an open circuit voltage (V_{oc}) of 1.66 V. Given that the corresponding CIGS mini-module comprises four unit cells connected in series, this V_{oc} value is notably low. The deviation in V_{oc} could be attributed to one of the unit cells being bypassed due to the shunt path. A bypassed unit cell has minimal contribution to the overall device voltage, which can influence the performance of the entire modular device.

Figure 4 presents the results of biased thermography analysis, indicating the potential for enhancing the signal from shunt defects either through the application of a high-voltage bias or prolonged bias exposure. The thermography images in Figure 4a,b under a +6 V and +7 V bias, respectively, employ a temperature scale of 10–70 °C. By contrast, the thermography images in Figure 4c,d under −6 V and −7 V bias, respectively, employ a temperature scale of 20–30 °C. A detailed examination of thermal variations in the regions marked A to E in Figure 4a–d was conducted with respect to the applied positive and negative biases (Figure 4e,f).

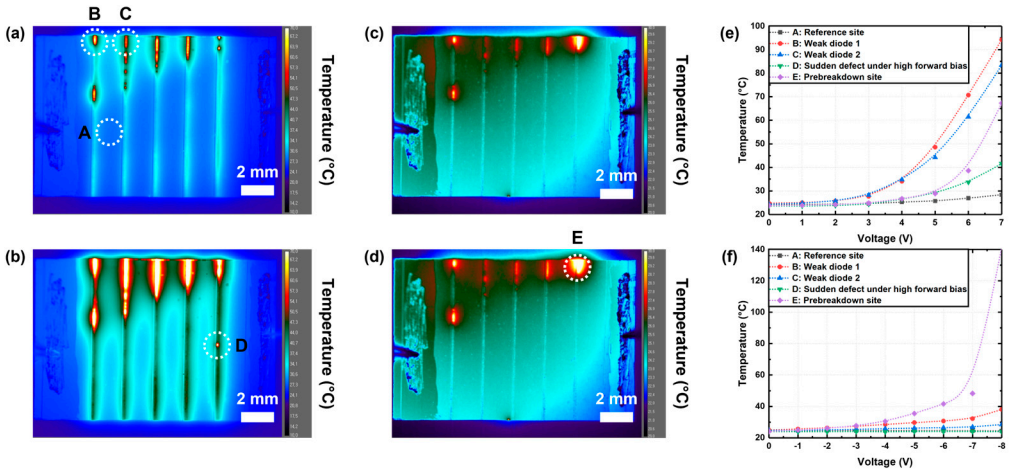

Figure 4. Visualization and assessment of shunt defects through biased thermography. Thermography images with positive biases of +6 V (**a**) and +7 V (**b**) adopt a temperature scale of 10–70 °C, while images with negative biases of −6 V (**c**) and −7 V (**d**) use a temperature scale of 20–30 °C. The corresponding thermal variations for the marked regions A–E shown in images (**a**–**d**) were evaluated according to the applied positive and negative biases, the results of which are depicted in (**e**,**f**), respectively.

These thermographic images (Figure 4a–d) reveal a range of shunt defects, each manifesting different thermal behaviors under the applied bias. For instance, Regions B and C in Figure 4a indicate weak diode shunt behavior, with the temperature rising exponentially under forward bias alongside an increase in the voltage and exhibiting a relatively minor increase under reverse bias. By contrast, the defect in Region D, Figure 4b, remains invisible under low-voltage conditions, appears abruptly under high voltage, and is absent under reverse bias. Region E, as depicted in Figure 4d, shows a pre-breakdown site, demonstrating a drastic rise in temperature under high-reverse-bias conditions. At −7 V, the temperature was approximately −38.3 °C but swiftly increased to 141.3 °C at −8 V.

Subjecting the sample to elevated temperatures over an extended period during thermography analysis can lead to irreversible damage to the device. Consequently, while a high applied bias can enhance the visibility of shunt sites, it poses a risk of permanent damage. Given this aspect, the LIT analysis is more valuable as it utilizes a brief pulsed bias to produce the thermal signal, representing a more viable nondestructive analysis method for shunt site detection than the method in which the sample is exposed to a high and

continuous voltage bias for an extended duration. Nevertheless, the temporal temperature profile monitoring offered by biased thermography can provide valuable insights into the thermal behavior of defects under various voltage conditions.

In Figure 4, a noticeable difference between the subcells in panels (a) and (b) can be observed as opposed to those in panels (c) and (d). Notably, all the panels depict segments from an identical CIGS mini-module, each comprising five unit cells. The nuanced appearance of the rightmost unit cell, exclusively isolated by P3, makes it less visibly pronounced in panels (a) and (b). In terms of the electrode characteristics, the current in the electrode, designated as negative, flowed to the adjacent cells primarily through the TCO due to the isolation of the back electrode. By contrast, the current in the electrode designated as positive predominantly flowed through Mo, given the non-isolated state of the back electrode (Figure 5). This distinct current pathway mitigated heat generation due to the sheet resistance of TCO, which is otherwise manifested in the four other cells. These observations demonstrate the intricate dynamics of the structural and electrical factors, influencing both the operational behavior and visual representation of unit cells under distinct voltage conditions.

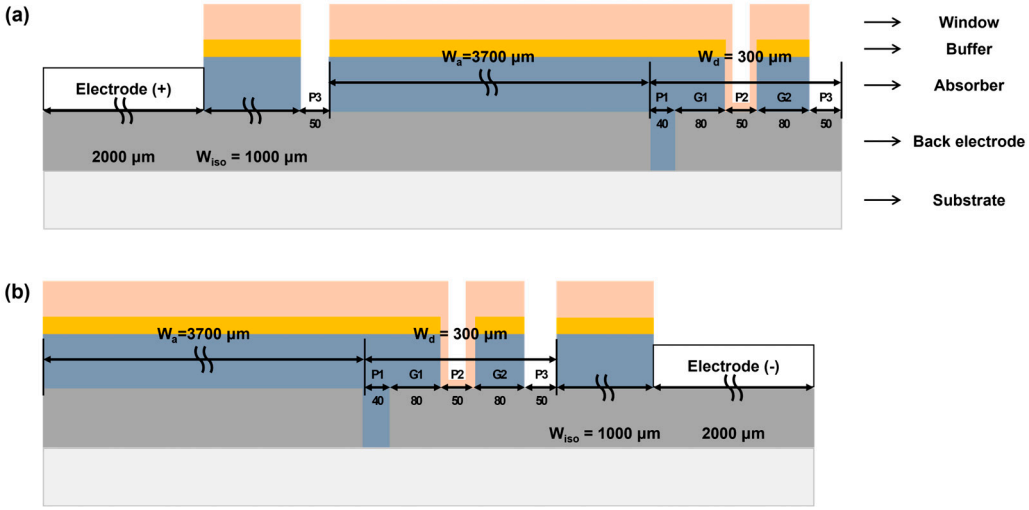

Figure 5. Schematic of the distinctions between positive (**a**) and negative electrode (**b**) sections within the CIGS mini-module. These numerical specifications might differ between the individual samples. Notations: W_{iso} (width of isolation area), W_a (width of active area), W_d (width of dead area), P1, P2, P3 (first, second, and third patterns), and G1, G2 (gaps between patterns).

Figure 6 presents a comparison of CIGS mini-modules under distinct shunt conditions. The LIT image in Figure 6a depicts a scenario with rare occurrences of critical shunt sites. The LIT image in Figure 6b shows frequent shunt sites throughout the sample. Photovoltaic performance parameters for these cases are delineated in Figure 6c,d.

For mini-modules with minimal shunting, as evident from Figure 6a, the shunt resistance loss remains marginal. Consequently, both the open-circuit voltage (V_{oc}) and fill factor (FF) are moderately retained post-modularization, as illustrated in Figure 6c. Conversely, when frequent shunting is observed (Figure 6b), there is a notable decline in the fill factor (FF), which is accompanied by a significant loss in V_{oc} due to leakage, thus confirming a direct correlation between the prevalence of shunt sites and a corresponding reduction in efficiency—a relationship further elucidated by juxtaposing LIT images with the J–V curves.

The origin of these shunt sites can be mainly attributed to local absorber delamination and fracture, triggering an ohmic shunt due to the partial short-circuiting of the top and bottom electrodes. Comprehensive insights into the causative factors of shunt sites and prospective countermeasures have been discussed in our previous report [15].

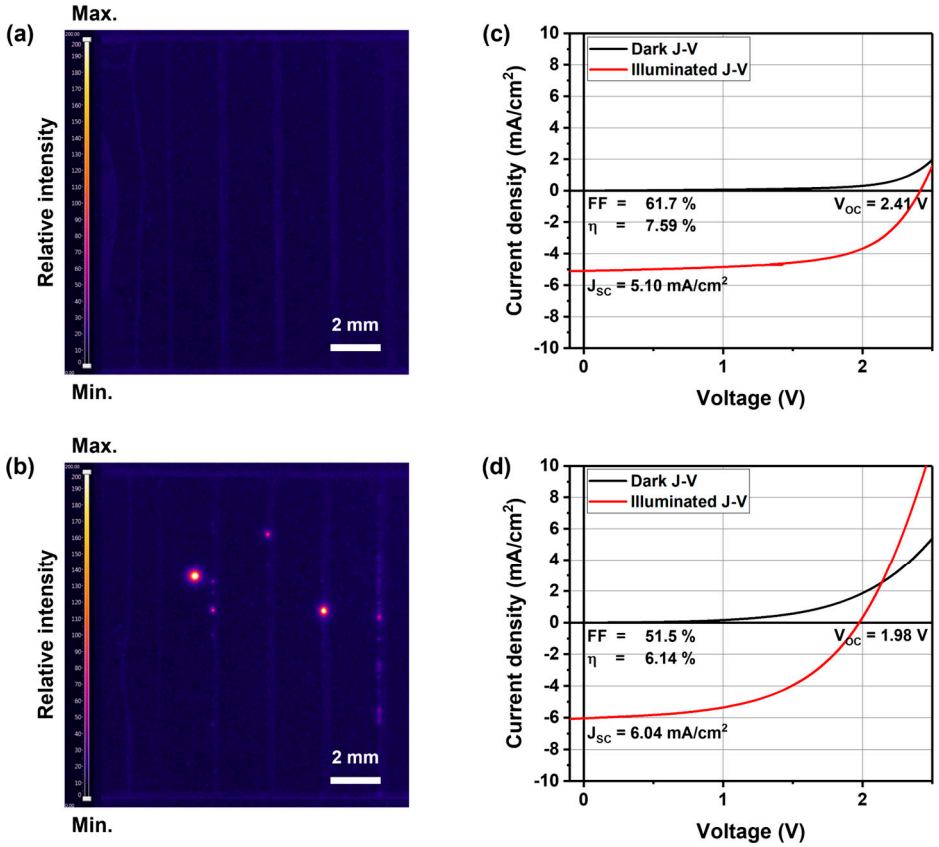

Figure 6. LIT images and corresponding J–V characteristic curves of CIGS mini-modules with an area of 2.06 cm^2 and varied shunt site occurrences: (**a**) LIT image showing minimal shunt sites. (**b**) LIT image showing frequent shunt sites. (**c**) J–V characteristic curve associated with (**a**). (**d**) J–V characteristic curve corresponding to (**b**).

4. Discussion

A comprehensive, empirical comparison was conducted between biased thermography and LIT to diagnose shunt defects in CIGS modules in this study, primarily aiming to determine the strengths and limitations inherent to each method to provide guidelines for method selection and optimization based on specific application requirements. A system capable of both biased thermography and LIT was used to analyze CIGS mini-modules. The comparison results highlight the effectiveness of LIT and suggested scenarios in which biased thermography might be a viable alternative.

The findings of this analysis demonstrate the influence of the temperature resolution for the infrared (IR) camera on noise generation while also revealing how signals resulting from applied bias could be discriminated from inherent noise. LIT could significantly enhance the signal-to-noise ratio, improving defective visibility, resolution, and quantification. By contrast, biased thermography exhibited a baseline bias independent of the externally applied bias, which could be attributed to the measurement environment. We devised strategies to effectively mitigate this bias.

This study demonstrates the potential of LIT to enhance the signals of defects that exhibit weak thermal behavior. We found LIT to be a more effective technique for identifying and analyzing such defects. By contrast, applying a strong bias in biased thermography, while effective at enhancing the signal, comes with limitations. The analysis further revealed a range of thermal behaviors associated with different types of defects that could be present in solar cell samples.

5. Conclusions

In conclusion, this study provides useful insights into the relative merits of biased thermography and LIT when diagnosing shunt defects in CIGS modules. LIT is recommended for its ability to detect subtle thermal behaviors of defects and enhance the signal-to-noise ratio, resulting in improved defect visibility, resolution, and quantification. Biased thermography could be a cost-effective alternative when its limitations are understood, meaning appropriate measures can be taken to enhance its performance.

Author Contributions: S.H.L. led and conceived the project, set up the bias and lock-in thermography measurement system, and performed the measurements and analyses. H.-S.L., D.K. and Y.K. contributed to the interpretation of the data and provided critical revisions to the manuscript. Y.K. supervised the project. All authors have read and agreed to the published version of the manuscript.

Funding: This work was supported by the New & Renewable Energy Core Technology Program of the Korea Institute of Energy Technology Evaluation and Planning (KETEP) from the Ministry of Trade, Industry, and Energy [grant number 20214000000680]. This work was supported by "Human Resources Program in Energy Technology" of the Korea Institute of Energy Technology Evaluation and Planning (KETEP) and granted financial resource from the Ministry of Trade, Industry & Energy, Republic of Korea. (No. 20204010600470). This work was supported by the KU-KIST Graduate School Project.

Data Availability Statement: Not applicable.

Conflicts of Interest: The authors declare no competing interests.

Abbreviations

CBD, chemical bath deposition; CIGOX, Cu–In–Ga-mixed oxide; CIGS, copper indium gallium selenide; LIT, lock-in thermography; P1, first pattern; P2, second pattern; P3, third pattern; RF, radio frequency; ROI, regions of interest.

References

1. Ren, A.; Xu, H.; Zhang, J.; Hung, H.; Delamarre, A.; Watanabe, K.; Zhang, J.; Wu, L.; Liu, C.; Sugiyama, M. Spatially resolved identification of shunt defects in thin film solar cells via current transport efficiency imaging combined with 3D finite element modeling. *Sol. RRL* **2019**, *3*, 1800342. [CrossRef]
2. Puranik, V.E.; Kumar, R.; Gupta, R. Generalized quantitative electroluminescence method for the performance evaluation of defective and unevenly degraded crystalline silicon photovoltaic module. *Prog. Photovolt.* **2023**, *31*, 269–282. [CrossRef]
3. Koester, L.; Lindig, S.; Louwen, A.; Astigarraga, A.; Manzolini, G.; Moser, D. Review of photovoltaic module degradation, field inspection techniques and techno-economic assessment. *Renew. Sustain. Energy Rev.* **2022**, *165*, 112616. [CrossRef]
4. Nofal, S.; Pieters, B.E. A novel non-destructive characterization method to investigate hot-spot formation in CIGS solar cells using lock-in thermography. In Proceedings of the 48th Photovoltaic Specialists Conference (PVSC), Fort Lauderdale, FL, USA, 20–25 June 2021. [CrossRef]
5. Breitenstein, O.; Sturm, S. Lock-in thermography for analyzing solar cells and failure analysis in other electronic components. *Quant. InfraRed Thermogr. J.* **2019**, *16*, 203–217. [CrossRef]
6. Breitenstein, O.; Warta, W.; Langenkamp, M. *Thermography: Basics and Use for Evaluating Electronic Devices and Materials*; Springer: Berlin/Heidelberg, Germany, 2010.
7. Sinha, A.; Bliss, M.; Wu, X.; Roy, S.; Gottschalg, R.; Gupta, R. Cross-characterization for imaging parasitic resistive losses in thin-film photovoltaic modules. *J. Imaging* **2016**, *2*, 23. [CrossRef]
8. Breitenstein, O.; Frühauf, F.; Bauer, J. Advanced local characterization of silicon solar cells. *Phys. Status Solidi* **2017**, *214*, 1700611. [CrossRef]
9. Schubert, M.C.; Mundt, L.E.; Walter, D.; Fell, A.; Glunz, S.W. Spatially resolved performance analysis for perovskite solar cells. *Adv. Energ. Mater.* **2020**, *10*, 1904001. [CrossRef]
10. Fecher, F.W.; Adams, J.; Vetter, A.; Buerhop-Lutz, C.; Brabec, C.J. Loss analysis on CIGS-modules by using contactless, imaging illuminated lock-in thermography and 2D electrical simulations. In Proceedings of the 40th Photovoltaic Specialist Conference (PVSC), Denver, CO, USA, 8–13 June 2014; Volume 2014, pp. 3331–3334. [CrossRef]
11. Guthrey, H.; Nardone, M.; Johnston, S.; Liu, J.; Norman, A.; Moseley, J.; Al-Jassim, M. Characterization and modeling of reverse-bias breakdown in Cu (In, Ga) Se2 photovoltaic devices. *Prog. Photovolt. Res. Appl.* **2019**, *27*, 812–823. [CrossRef]
12. Aninat, R.; Bakker, K.; Jouard, L.; Ott Cruz, M.G.S.; Yilmaz, P.; Theelen, M. Extraction and microscopic analysis of partial shading-induced defects in a commercial CIGS PV module. *Prog. Photovolt. Res. Appl.* **2022**, *30*, 1101–1114. [CrossRef]

13. Palmiotti, E.; Johnston, S.; Gerber, A.; Guthrey, H.; Rockett, A.; Mansfield, L.; Silverman, T.J.; Al-Jassim, M. Identification and analysis of partial shading breakdown sites in CuInxGa(1-x)Se2 modules. *Sol. Energy* **2018**, *161*, 1–5. [CrossRef]
14. Bin Mo, C.; Park, S.J.; Bae, S.; Lim, M.H.; Nam, J.; Kim, D.; Yang, J.; Suh, D.; Min, B.K.; Kim, D.; et al. Impact of buffer layer process and Na on shunt paths of monolithic series-connected CIGSSe thin film solar cells. *Sci. Rep.* **2019**, *9*, 3666. [CrossRef] [PubMed]
15. Lee, S.H.; Kim, M.K.; Bae, S.; Nam, J.; Park, H.; Lee, S.; Jang, Y.J.; Min, B.K.; Yang, J.; Kang, Y.; et al. Absorber delamination-induced shunt defects in alcohol-based solution-processed Cu (In, Ga)(S, Se)2 solar modules. *ACS Appl. Energy Mater.* **2020**, *3*, 10384–10392. [CrossRef]
16. Kingma, A.; Naziris, F.; Bakker, K.; Mack, K.; Huhn, V.; Theelen, M. Study of the physical and chemical origin of features observed in luminescence and thermography images of Cu(In, Ga)Se2. *Sol. Energy Mater. Sol. Cells* **2021**, *230*, 111145. [CrossRef]
17. Kumar, N.M.; Chopra, S.S.; de Oliveira, A.K.V.; Ahmed, H.; Vaezi, S.; Madukanya, U.E.; Castañón, J.M. Solar PV module technologies. In *Photovoltaic Solar Energy Conversion*; Elsevier: Amsterdam, The Netherlands, 2020; pp. 51–78. [CrossRef]
18. Eltuhamy, R.A.; Rady, M.; Ibrahim, K.H.; Mahmoud, H.A. Novel features extraction for fault detection using thermography characteristics and IV measurements of CIGS thin-film module. *Instrum. Mes Métrol.* **2020**, *19*, 311–325. [CrossRef]
19. Kim, Y.; Shin, M.; Lee, M.-J.; Kang, Y. Hot-spot generation model using electrical and thermal equivalent circuits for a copper indium gallium selenide photovoltaic module. *Sol. Energy* **2021**, *216*, 377–385. [CrossRef]

Disclaimer/Publisher's Note: The statements, opinions and data contained in all publications are solely those of the individual author(s) and contributor(s) and not of MDPI and/or the editor(s). MDPI and/or the editor(s) disclaim responsibility for any injury to people or property resulting from any ideas, methods, instructions or products referred to in the content.